Solidification Paths and Phase Components at High Temperatures of High-Zn Al-Zn-Mg-Cu Alloys with Different Mg and Cu Contents

W.X. SHU, L.G. HOU, J.C. LIU, C. ZHANG, F. ZHANG, J.T. LIU, L.Z. ZHUANG, and J.S. ZHANG

Studies were carried out systematically on a series of Al-8.5 wt pct Zn-xMg-yCu alloys (x is about 1.5, 2.0, and 2.5 wt pct, and y is about 1.5, 2.0, 2.5, and 2.9 wt pct). The effects of alloying elements Mg and Cu on the microstructures of as-cast and homogenized alloys were investigated using the computational/experimental approach. It shows that $Mg(Zn,Al,Cu)_2$ (σ) phase can exist in all the as-cast alloys without any observable $Mg_{32}(Al,Zn)_{49}/Al_2Mg_3Zn_3$ (T) or Al_2CuMg (S) phase, whereas Al_2Cu (θ) phase is prone to exist in the alloys with low Mg and high Cu contents. Thermodynamic calculation shows that the real solidification paths of the designed alloys fall in between the Scheil and the equilibrium conditions, and close to the former. After the long-time homogenization [733 K (460 °C)/168 hours] and the two-step homogenization [733 K (460 °C)/24 hours + 748 K (475 °C)/24 hours], the phase components of the designed alloys are generally consistent with the calculated phase diagrams. At 733 K (460 °C), the phase components in the thermodynamic equilibrium state are greatly influenced by Mg content, and the alloys with low Mg content are more likely to be in single-Al phase field even if the alloys contain high Cu content. At 748 K (475 °C), the dissolution of the second phases is more effective, and the phase components in the thermodynamic equilibrium state are dominated primarily by (Mg + Cu) content, except the alloys with (Mg + Cu) $\gtrsim$ 4.35 wt pct, all designed alloys are in single-Al phase field.

I. INTRODUCTION

THE Al-Zn-Mg-Cu series aluminum alloys are widely used as structural parts in the aeronautics industry for their high mechanical properties[1,2] and to compete with growing utilization of composite materials (*e.g.*, graphite epoxy composites),[3] further improving the properties such as static strength, damage tolerance, and corrosion resistance, is still greatly desired for these high-strength aluminum alloys.[4] As the key strengthening method, increasing Zn and/or Mg content can contribute greatly to the formation of the major strengthening phases (*e.g.*, GP zone, η' and η phases), and undoubtedly this will enhance the strength of the Al-Zn-Mg-Cu series alloys (the η phase represents the equilibrium precipitates with the hexagonal structure

$MgZn_2$, it has been widely shown that some substitution of Cu and Al occurs at the Zn sublattice, and the chemical composition $Mg(Zn,Al,Cu)_2$ has been proposed in Cu-containing 7xxx series Al alloys).[5] With high solubility in the Al matrix, very high Zn content (*e.g.*, 10 wt pct or more) can be fully dissolved into Al matrix of the Al-Zn-Mg-Cu system at 733 K (460 °C) through optimizing the composition.[6,7] However, Mg content in the commercial Al-Zn-Mg-Cu alloys is usually controlled below 2.6 wt pct in consideration of solid-solubility limitation and possible destructive influence on fracture toughness. For the newly registered Al-Zn-Mg-Cu alloys with high strength and toughness (*e.g.*, AA 7056, AA 7095, and AA 7155), low quench sensitivity (*e.g.*, AA 7037), or super high-strength (*e.g.*, AA 7168 and AA 7136), higher Zn content (7.6 to 9.8 wt pct) is an obvious characteristic, accompanied with higher total (Zn + Mg + Cu) solute contents (with lower limit 9.7 to 12.1 wt pct).[8] However, Al-Zn-Mg-Cu alloys with high alloying levels are usually difficult to be fully homogenized/solid-solution treated for the existence of lots of coarse intermetallic particles in the as-cast/deformed alloys. These undissolved coarse particles can affect hot workability and recrystallization behavior, as well as damage strength, fracture toughness, fatigue, and anticorrosion performances directly or indirectly.[9–11] The typical intermetallic phases include unsoluble phases (*e.g.*, Al_7Cu_2Fe, *etc.*), partially soluble phases (*e.g.*, Mg_2Si, *etc.*), and soluble phases (*e.g.*, σ, θ,

W.X. SHU, Doctor Candidate, L.G. HOU, Research Assistant, J.C. LIU, Postdoctor, and L.Z. ZHUANG and J.S. ZHANG, Professors, are with the State Key Laboratory for Advanced Metals & Materials, University of Science and Technology Beijing, Beijing 100083, P.R. China. Contact e-mail: lghou@skl.ustb.edu.cn C. ZHANG, Materials Scientist, and F. ZHANG, President, are with CompuTherm LLC, Madison, WI 53706. J.T. LIU, Doctor Candidate, is with the State Key Laboratory for Advanced Metals & Materials, University of Science and Technology Beijing, and also with the State Key Laboratory for Fabrication and Processes of Nonferrous Metals, General Research Institute for Nonferrous Metals, Beijing 100088, P.R. China.

T, and S phases, *etc.*) (the σ phase represents the intermetallic compound particles in microsize with the hexagonal structure $MgZn_2$, and its chemical composition can also be described as $Mg(Zn,Al,Cu)_2$ because of the substitution of Cu and Al at the Zn sublattice).[12,13] The unsoluble or partially soluble phases induced by impurity elements (*e.g.*, Fe and Si, *etc.*) are hard to be eliminated during manufacture, and controlling the impurity contents in the as-cast alloys could be an effective way to reduce them. The soluble phases can be dissolved fully or partly through homogenization or solid-solution treatment, and the effects depend on heat treatments and alloy compositions. Nowadays, new casting, heat treatment, and thermal–mechanical techniques have been developed; however, composition optimization is still the most effective way to control the soluble intermetallic phases.[14–16]

For commercial alloys, a basic understanding of their solidification paths, namely the phase formation sequences during solidification, is very important for alloy design and processing improvement because the complex phase transformations during solidification could make the microstructure/property design to be very difficult because of the uncertainties involved.[17] Many investigations have been focused on the phase components of as-cast Al-Zn-Mg-Cu alloys so far, but different combinations of σ, T, S, and θ phases have been regarded as the phase components of the as-cast alloys (the impurity phases, *e.g.*, Al_7Cu_2Fe and Mg_2Si, are not considered here).[12,18–21] For example, σ and S phases were observed in the as-cast and homogenized 1973 Al alloy;[21] σ, T, S, and possible θ phases were found in a series of as-cast alloys within the AA 7055 Al alloy composition window.[20] Also, σ, S, and θ phases were observed in as-cast AA 7050 Al alloy,[12] but only σ phase was found in as-cast AA 7150 and AA 7010 Al alloys.[18,19] Therefore, how to judge or predict the phase

components under designed alloy compositions should be very important with an urgent requirement, and in-depth study of this point should be systematically and precisely performed.

In this study, the computational/experimental approach[22,23] was employed to investigate the solidification paths and the phase components after typical industrial homogenization treatments of a series of Al-Zn-Mg-Cu alloys with high Zn content (about 8.5 wt pct) and different Mg/Cu content. The Pandat software package (CompuTherm LLC, Madison, WI)[24] was used in this work to perform solidification and phase equilibria simulations. The simulated results coupled with the experimental data can provide better understanding of the effects of Mg/Cu content on solidification paths and phase components at high temperatures of high-Zn Al-Zn-Mg-Cu alloys.

II. EXPERIMENTAL DETAILS AND METHODS

All the present alloys were prepared with high-purity Al (99.99 pct), Zn (99.99 pct), Mg (99.99 pct) metals, Al-50Cu, Al-10Zr, and Al-10Ti master alloys, as well as Al-5Ti-B refiner. The original materials were melted in an electrical-resistance furnace and the melts were poured into a water-cooled steel mold to get the ingots with sizes about $210 \times 120 \times 100$ mm. The compositions of the ingots were controlled by optical emission spectrometer ARL 4460 (ThermoFisher Scientific, Waltham, MA), and the results are shown in Table I. The impurity levels of Fe and Si elements in the as-cast alloys were controlled below 0.02 and 0.01 wt pct, respectively. It is beneficial for the study of the influences of the main alloying elements on the solidification paths as well as the phase components at different heat-treatment

Table I. Chemical Compositions of the Experimental Alloys in Weight Percent (and Atmospheric Percent)

No.	Zn	Mg	Cu	Zr	Ti	Fe	Si	Zn + Mg + Cu	Zn:Mg Ratio	Cu:Mg Ratio
1-1	8.58	1.41	1.47	0.11	0.02	<0.02	<0.01	11.46	6.09	1.04
	(3.78)	(1.68)	(0.66)	(0.03)	(0.01)	(<0.01)	(<0.01)	(6.12)	(2.25)	(0.39)
1-2	8.52	1.47	1.92					11.91	5.80	1.31
	(3.76)	(1.76)	(0.86)					(6.38)	(2.14)	(0.49)
1-3	8.74	1.50	2.45					12.69	5.83	1.63
	(3.88)	(1.80)	(1.10)					(6.78)	(2.16)	(0.61)
1-4	8.73	1.41	2.90					13.04	6.19	2.06
	(3.89)	(1.70)	(1.31)					(6.90)	(2.29)	(0.77)
2-1	8.76	2.06	1.51					12.33	4.25	0.73
	(3.86)	(2.46)	(0.68)					(7.00)	(1.57)	(0.28)
2-2	8.64	1.97	2.05					12.66	4.39	1.04
	(3.82)	(2.36)	(0.92)					(7.10)	(1.62)	(0.39)
2-3	8.59	2.00	2.44					13.03	4.30	1.22
	(3.80)	(2.40)	(1.10)					(7.30)	(1.58)	(0.46)
3-1	8.57	2.52	1.42					12.51	3.40	0.56
	(3.77)	(3.00)	(0.63)					(7.40)	(1.26)	(0.21)
3-2	8.61	2.47	1.90					12.98	3.49	0.77
	(3.80)	(2.95)	(0.85)					(7.60)	(1.29)	(0.29)
3-3	8.67	2.50	2.50					13.67	3.47	1.00
	(3.84)	(3.00)	(1.13)					(7.97)	(1.28)	(0.38)

Alloy 2-3 was studied in Ref. [25], and its XRD and DSC results are referenced in this article.

temperatures, and it is beneficial for the improvement of mechanical properties.

Specimens (size: 12 × 12 × 12 mm) were cut from the quarter-thickness position of the ingots referring to the sampling location of the ingots on industrial scale,[26] although no obvious macrosegregation was found in the transverse sections of the present ingots because of the relatively small sizes of the ingots and the high solidification rate (approximately 2 to 3 K/second [2 to 3 °C/ second]). The specimens were homogenized with designed conditions to simulate typical industrial practices, and the treatments were performed in an air furnace with temperature accuracy of ±2 K (2 °C). The specimens were heated with 30 K/hour (30 °C/hour) to the homogenization temperature of 733 K (460 °C) for 24 hours. After homogenization, the samples were quenched into room-temperature water quickly to obtain the high-temperature microstructures for analysis. For the alloys that cannot be homogenized fully after this single-step homogenization, a two-step homogenization process [733 K (460 °C)/24 hours + 748 K (475 °C)/24 hours] was designed to eliminate the residual intermetallic particles with 15 K/hour (15 °C/hour) heating rate from 733 K to 748 K (460 °C to 475 °C). Moreover, a long-time homogenization process [733 K (460 °C)/168 hours] was also used to achieve the equilibrium phase components of these alloys at 733 K (460 °C). The treating temperatures of the single- and two-step homogenizations were chosen based on the differential scanning calorimetry (DSC) results that were obtained from TA2910 DSC instrument by the 10 K/minute (10 °C/minute) heating rate. The DSC samples were 3-mm-diameter disks with mass of approximately 10 mg, and a baseline scan was recorded from a super pure Al sample and was subsequently subtracted from the alloy scans.

Color metallography was used in the light microscope (LM) to distinguish different grains and make a relatively precise measurement of the grain size. For conventional optical examination, the specimens were mechanical polished and etched with Keller's reagent. The scanning electron microscopy (SEM) observation was conducted in a ZEISS LEO 1450 SEM (Carl Zeiss, Oberkochen, Germany) equipped with the energy dispersive X-ray spectroscopy (EDS) Kevex SIGMA (resolution: 139 eV at MnKα; Noran Instruments Inc., Middleton, WI). The X-ray diffraction (XRD) analysis was performed on a Rigaku D_{MAX}-RB X-ray diffractometer (Cu Kα; working voltage: 40 kV; step length: 0.02 deg; scanning rate: 9 deg/minute; Rigaku Corporation, Tokyo, Japan).

III. RESULTS AND DISCUSSION

A. *Phase Components and Solidification Paths of the As-Cast Alloys*

Typical dendritic Al matrices with statistical average grain sizes of 190 to 240 μm (239, 231, 216, and 190 μm for as-cast alloys 1-1, 1-3, 3-1, and 3-3, respectively) are shown in Figures 1(a) through (d). Obviously, the grain sizes are reduced with increasing amounts of solutes (especially Mg solute), which is consistent with the results presented in Reference 20. Figures 1(e) and (f) show the interdendritic eutectic structures of as-cast alloy 3-3. It is clear that the coarse second phases are distributed on the dendrite boundaries that comprise the shell.

Figure 2 shows two typical SEM images of the as-cast alloys, and it is clear that two different intermetallic phases with different contrasts (white and gray) appear in alloy 1-4, whereas only white phase can be found in alloy 3-1. Actually, the whole SEM observation shows that the white phase exists in all the designed alloys, whereas the gray phase exists only in alloys 1-1, 1-2, 1-3, 1-4, 2-2, and 2-3. The compositions (Table II) of the marked phases in Figure 2 as well as some white/gray phase in other alloys show that the composition of the white phase is approximately 33 to 35 at. pct Mg, 18 to 30 at. pct Al, 12 to 19 at. pct Cu, and 21 to 33 at. pct Zn. The gray phase contains approximately 66 to 69 at. pct Al, 27 to 30 at. pct Cu, 1 to 3 at. pct Mg, and 1 to 2 at. pct Zn. It is noted that the Mg atoms in the white phase take up approximately one third of the total atoms in all cases (the same phenomenon has been observed for the near-equilibrium η precipitates with structure of $MgZn_2$[5]), and the compositions of these white phases are close to the concentration of σ phase,[27] which can always be observed in as-cast Al-Zn-Mg-Cu alloys. The region D (Figure 2(b)) gives an average composition of the (Al + σ) eutectic, and its alloying element concentrations are approximately half of those of σ phase because of higher Al content from Al matrix to the compounds for the use of energy spectrum. The Al:Cu atom ratios of the gray phases with few dissolved Zn and Mg atoms are approximately 2.0, and it is deduced to be Al_2Cu (θ) phase.[27] Moreover, a common phenomenon for the alloys containing θ phase is that the θ phase always adjoins the σ phase, indicating the θ phase was solidified as the (Al + σ + θ) eutectic.

The XRD patterns in Figure 3(a) show only σ phase with crystal structure $MgZn_2$ can be detected in all the as-cast alloys without any signal of θ phase for its small concentration. The intensity of the diffraction peaks of σ phase becomes stronger with increasing amount of solutes.

The DSC tests show that two endothermic peaks [Peak I around 738 K (465 °C) and Peak II around 748 K (475 °C)] appear for as-cast alloys 1-1, 1-2, 1-3, 1-4, 2-2, and 2-3, whereas only one endothermic peak (Peak II) appears for as-cast alloys 2-1, 3-1, 3-2, and 3-3 (Figure 3(b)). As is well known, Peak II is attributed to the melting of the (Al + σ) eutectic,[28] more intrinsically this endothermic reaction can be regarded as the gradual dissolution of σ phase with heating. However, there is no clear explanation about the reaction related to Peak I in the existing literature. To the authors' knowledge, it has been reported that Peak I is more likely to arise in the 7xxx Al alloys with high Zn content, but the related reaction has not been discussed.[29,30] According to the SEM observation above, it could be inferred preliminarily that Peak I would be related to the melting of the (Al + σ + θ) eutectic pockets, and this will be further
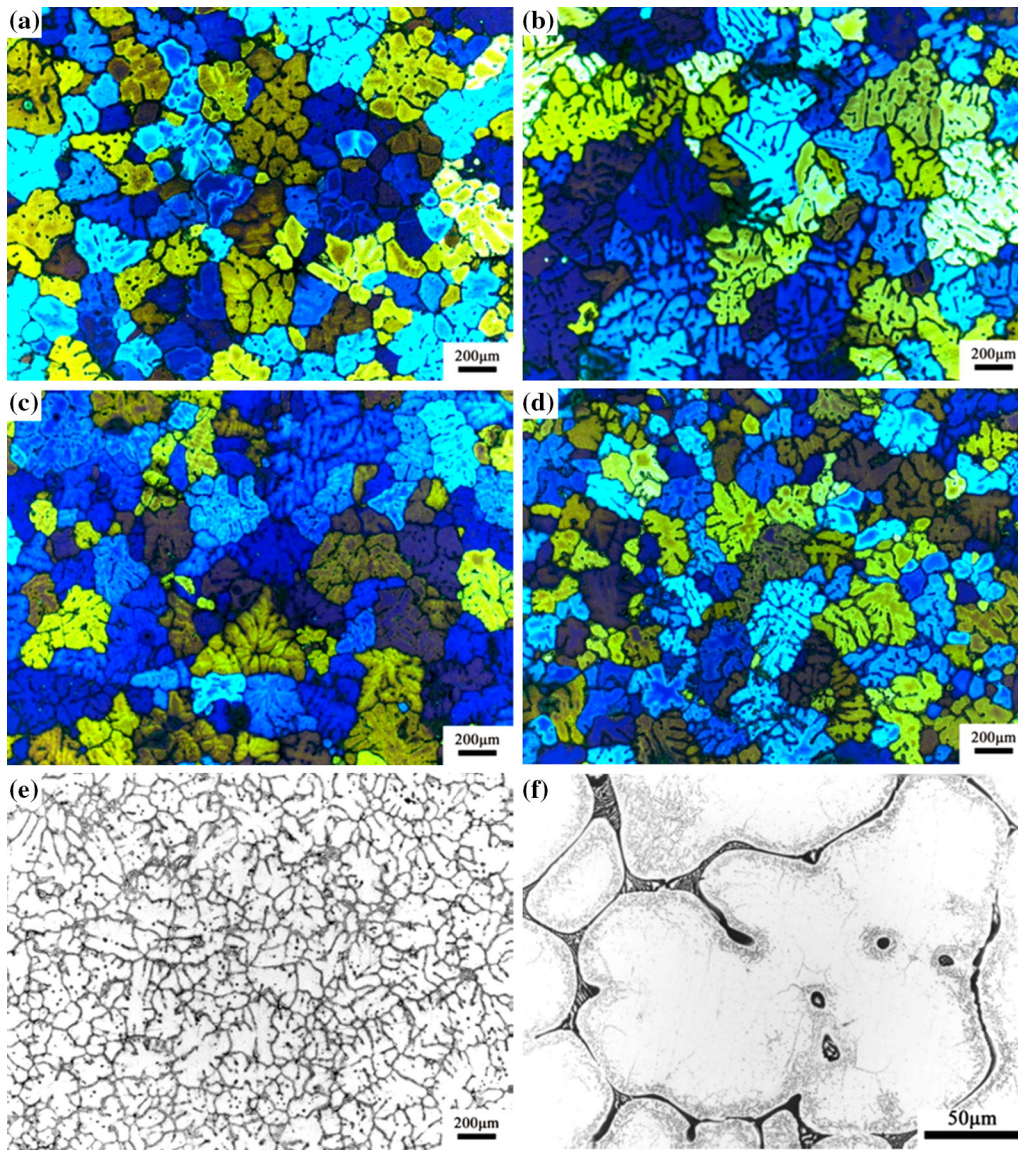
Fig. 1—Optical microstructures (in transverse section) of the as-cast alloys. Color micrographs of as-cast alloys (*a*) 1-1, (*b*) 1-3, (*c*) 3-1, and (*d*) 3-3; conventional micrographs of as-cast alloy 3-3 in (*e*) low magnitude and (*f*) high magnitude.

confirmed by the result of solidification simulation hereinafter, which shows the eutectic reaction Liq. $\rightarrow$ Al + σ + θ at ~738 K (465 °C) for some alloys in the Scheil model. Generally, for the 2xxx Al alloys, the peak temperature of the formation/melting of the (Al + θ) eutectic during DSC test is usually around 803 K to 823 K (530 °C to 550 °C);[31–34] thus, it can be inferred that the reaction associated with Peak I in Figure 3(b) cannot just be the melting of the (Al + θ) eutectic (or the dissolution of θ phase). Moreover, the calculated liquidus projection of Al-rich corner of the quaternary Al-Cu-Mg-Zn system in Reference 35 shows that the eutectic reaction Liq. $\rightarrow$ Al + θ occurs in the temperature range 778 K to 821 K (505 °C to 548 °C), whereas the four-phase equilibrium, Liq. + Al + σ + θ, starts below 740 K (467 °C). In summary, it is reasonable to associate Peak I with the melting of the (Al + σ + θ) eutectic pockets according to the current

SEM observation (Figure 2) and the thermodynamic principles.

The related peak temperature T_P and heat of reaction ΔH_R associated with phase transformation calculated from the DSC curves in Figure 3(b) are listed in Table III. It shows the T_P of the melting of the (Al + σ + θ) eutectic pockets (or the dissolution of the (σ + θ) pockets) is approximately 738 K (465 °C), whereas the T_P of the melting of the (Al + σ) eutectic (or the dissolution of the massive or "blocky" σ phase) is slightly fluctuant: approximately 750 K (477 °C) for the as-cast alloys with Mg content of approximately 2.0 and 2.5 wt pct, and approximately 747 K (474 °C) for the as-cast alloys with Mg content of approximately 1.5 wt pct. Nevertheless, no obvious regularity has been found between the changes of T_P and the composition variations of θ and σ phases. In general, deviations from the horizontal are indicative of solid-state reactions

accompanying heating, and the ΔH_R associated with an endothermic reaction can be proportional to the volume fraction of the phases dissolved.[36,37] From Table III, it can be seen that the ΔH_R associated with the massive σ phase dissolution is increased gradually with increasing amount of solutes (especially Mg solute), and the ΔH_R

associated with the $(\sigma + \theta)$ pockets dissolution is reduced greatly with increasing Mg content. It can be deduced that the amounts of the massive σ phase and the $(\sigma + \theta)$ pockets in the as-cast alloys are determined primarily by Mg content, i.e., the more the Mg content, the more the massive σ phase and the less the $(\sigma + \theta)$ pockets. For the alloys with similar Mg content, the more the Cu content, the more the massive σ phase, and generally the more the $(\sigma + \theta)$ pockets. However, it is still hard for the alloys with high Cu content to form $(\sigma + \theta)$ pockets if the alloys contain high Mg content. In addition, neither T nor S phase can be found in all the as-cast alloys, and the related reasons will be explained next.

With the microstructural examination above and ignoring the primary Al_3Zr phase that is hard to be detected by SEM/XRD/DSC tests, the solidification paths are Liq. $\rightarrow$ (Liq. + Al) $\rightarrow$ (Liq. + Al + σ) $\rightarrow$ (Liq. + Al + σ + θ) for alloys 1-1, 1-2, 1-3, 1-4, 2-2, and 2-3. However, the last reaction is excluded for alloys 2-1, 3-1, 3-2, and 3-3. Also, the solidification paths can be calculated by thermodynamic simulation, and before the following simulation, two points should be noted: First, the simulation will be carried out with the quarternary Al-Zn-Mg-Cu system because the influence of Zr on the solidification is not the present focus, and its influence on the phase transformation during solidification is little except the primary Al_3Zr formation. Second, in the Scheil model the finally formed phases with total mole fraction less than 0.002 are not discussed because they are difficult to be detected experimentally in the as-cast alloys unless extreme care is taken.[38]

The solidification paths in the Scheil model of several typical alloys (alloys 1-1, 1-3, 3-1, and 3-3) are shown in Figure 4(a), and the phase components of alloy 1-3 during solidification are noted. For alloy 1-3 (with low Mg and high Cu contents), Al, σ phase, and θ phase can be formed successively at 902 K, 755 K, and 738 K (629 °C, 482 °C, and 465 °C) during solidification, which is similar to the solidification path of alloy 3-3
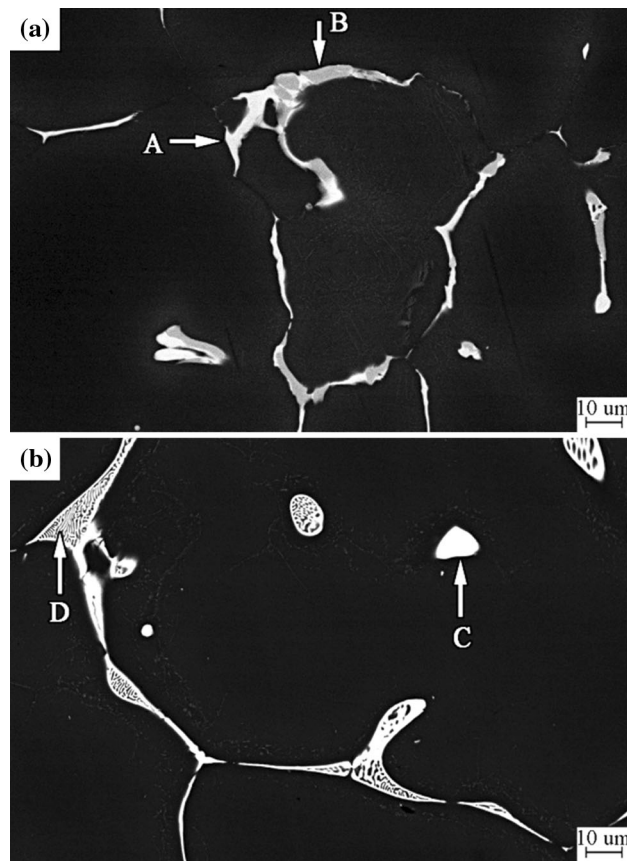

Fig. 2—Typical SEM images (in transverse section) of the as-cast alloys. Alloy (a) 1-4 and (b) 3-1.

Table II. Chemical Compositions (Atmospheric Percent) of the Intermetallic Phases in Fig. 2 as well as Some White/Gray Phase in Other As-Cast Alloys

| Alloy	Phase Marks	Mg	Al	Cu	Zn	Identified Phase
1-1	(white)	33.31	18.71	15.61	32.37	σ
	(gray)	1.57	67.40	29.50	1.54	θ
1-2	(white)	34.10	19.37	16.42	30.11	σ
	(gray)	1.76	68.19	28.78	1.27	θ
1-3	(white)	34.33	18.23	16.67	30.77	σ
	(gray)	1.36	67.67	29.01	1.96	θ
1-4	A	34.69	22.27	16.70	26.34	σ
	B	2.93	67.21	27.97	1.89	θ
2-1	(white)	33.81	29.16	15.26	21.77	σ
2-2	(white)	33.8	23.97	16.43	25.79	σ
	(gray)	2.41	66.77	29.07	1.76	θ
2-3	(white)	34.30	23.83	13.34	28.53	σ
	(gray)	1.69	68.55	28.28	1.48	θ
3-1	C	34.69	23.36	13.01	28.94	σ
	D	18.45	59.48	6.90	15.16	(Al + σ)
3-2	(white)	34.54	27.9	12.89	24.67	σ
3-3	(white)	33.67	23.47	18.17	24.68	σ
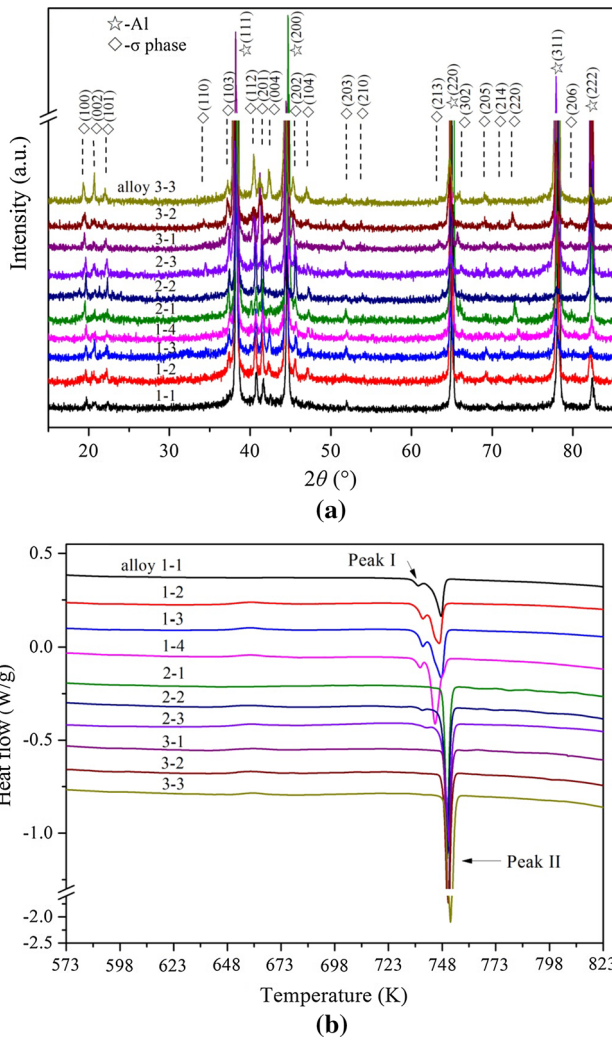
Fig. 3—(a) XRD patterns and (b) DSC curves of the as-cast alloys.

Table III. Peak Temperature T_P and Heat of Reaction ΔH_R Calculated From the DSC Curves (in Fig. 3(b)) of the As-Cast Alloys

Alloy	Peak I		Peak II	
	T_P (K)	ΔH_R (J/g)	T_P (K)	ΔH_R (J/g)
1-1	737.2	0.340	748.0	4.633
1-2	738.9	0.521	746.7	4.738
1-3	738.9	0.539	747.6	6.287
1-4	737.7	0.511	744.7	8.730
2-1	—	—	750.4	11.530
2-2	738.6	0.133	750.6	11.650
2-3	740.3	0.135	751.2	11.790
3-1	—	—	750.7	13.140
3-2	—	—	750.9	14.830
3-3	—	—	751.9	18.380

(with high Mg and Cu contents). Also, these three phases can be formed in alloy 1-1 (with low Mg and Cu contents) during solidification, but the bend indicating

the formation of θ phase is unobvious. Alloy 3-1 (with high Mg and low Cu contents) has no θ phase formed during solidification, and its solidification process will end at a higher temperature [753 K (480 °C)] than the other alloys [around 623 K (350 °C)].

To reveal the influences of alloy composition on solidification path, the composition evolutions in the liquids of alloys 1-1, 1-3, 3-1, and 3-3 during solidification in the Scheil model are shown in Figure 4(b), and some obvious features can be seen. First, the composition paths of alloys 1-1, 1-3, and 3-3 are similar; however, the composition path of alloy 3-1 is quite different. Second, although the initial Zn content of the liquid is only ~3.8 at. pct, it could be ~85 at. pct at the final stage of solidification for alloys 1-1, 1-3, and 3-3, showing an increase of one order of magnitude. This drastic composition variation should be the result of microsegregation during the course of solidification. In the following discussion, the solidification paths of alloys 1-1, 1-3, 3-1, and 3-3 are interpreted with the reference of Figure 4(b). For alloys 1-1, 1-3, and 3-3, Al phase starts to form when the temperature is decreased to the liquidus surface of the Al-Zn-Mg-Cu system at P0 [e.g., $P_{1-1}0$, $P_{1-3}0$, and $P_{3-3}0$, ~903 K (630 °C)], and the composition of the liquid follows the P0-P1 curve (e.g., $P_{1-1}0$-$P_{1-1}1$, $P_{1-3}0$-$P_{1-3}1$, and $P_{3-3}0$-$P_{3-3}1$) with gradually decreasing temperature. Once the liquid composition reaches P1 [e.g., $P_{1-1}1$, $P_{1-3}1$, and $P_{3-3}1$, ~758 K (485 °C)] on the (Liq. + Al + σ) three-phase surface of Al-Zn-Mg-Cu system, σ phase starts to solidify from the liquid and then the liquid composition will follow the P1–P2 curve (e.g., $P_{1-1}1$–$P_{1-1}2$, $P_{1-3}1$–$P_{1-3}2$, and $P_{3-3}1$–$P_{3-3}2$). When the liquid composition reaches P2 [e.g., $P_{1-1}2$, $P_{1-3}2$, and $P_{3-3}2$, ~738 K (465 °C)] on the monovariant four-phase equilibrium of the Al-Zn-Mg-Cu system,[35] Liq. + Al + σ + θ, the liquid composition will change its direction and follow the P2–P3 curve (e.g., $P_{1-1}2$–$P_{1-1}3$, $P_{1-3}2$–$P_{1-3}3$, and $P_{3-3}2$–$P_{3-3}3$). In the meantime, the θ phase can be formed and can coexist with (Liq. + Al + σ). From P3 [e.g., $P_{1-1}3$, $P_{1-3}3$, and $P_{3-3}3$, ~678 K (405 °C)] to PN [e.g., $P_{1-1}N$, $P_{1-3}N$, and $P_{3-3}N$, ~623 K (350 °C)], a series of complex reactions occur, but the corresponding heat evolutions and amounts of reaction products are little (mole fraction <0.002) so that the solidification during this stage is not discussed. Finally, the solidification ends at PN. For alloy 3-1, Al phase starts to form since $P_{3-1}0$ [900 K (627 °C)], and σ phase starts to form since $P_{3-1}1$ [763 K (490 °C)]. However, its trace of P1–P2 is far from those of other alloys as well as far from the four-phase equilibrium Liq. + Al + σ + θ, thus no θ phase can be formed during the whole solidification process. Finally, the solidification ends at $P_{3-1}2$ [753 K (480 °C)].

According to Figures 4(a) and (b), one can find that it is much more difficult for the alloys with low Cu content to form θ phase during solidification (e.g., alloy 1-1 and 3-1), especially the alloys with high Mg and low Cu contents (e.g., alloy 3-1). The calculated heat evolutions of alloy 1-4 (with lowest Mg and highest Cu contents) and alloy 3-1 (with highest Mg and lowest Cu contents) during solidification in the Scheil model are shown in Figure 4(c). Significant bends indicating the reactions of
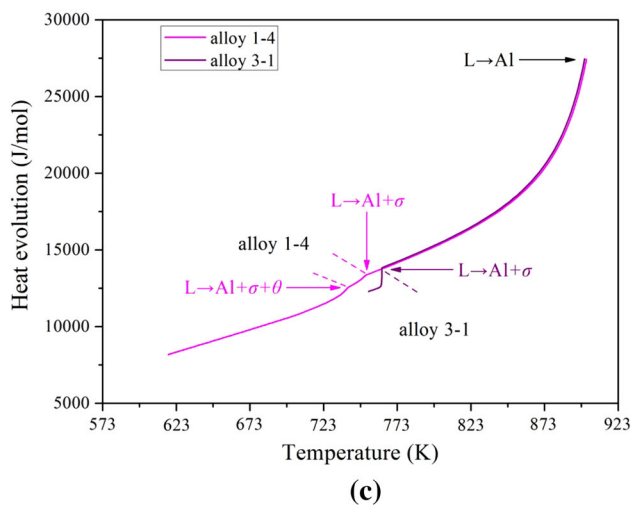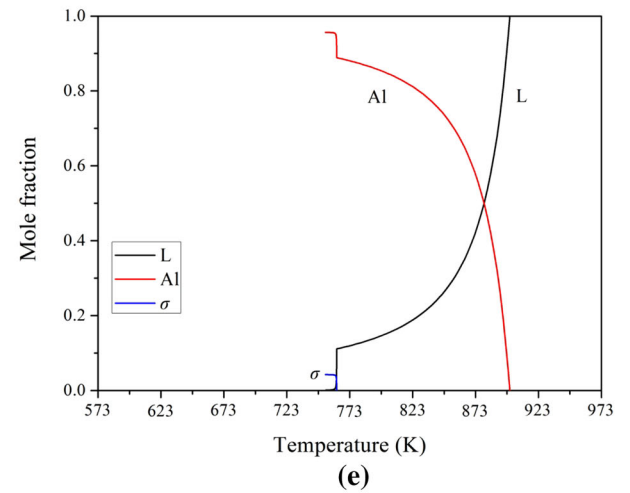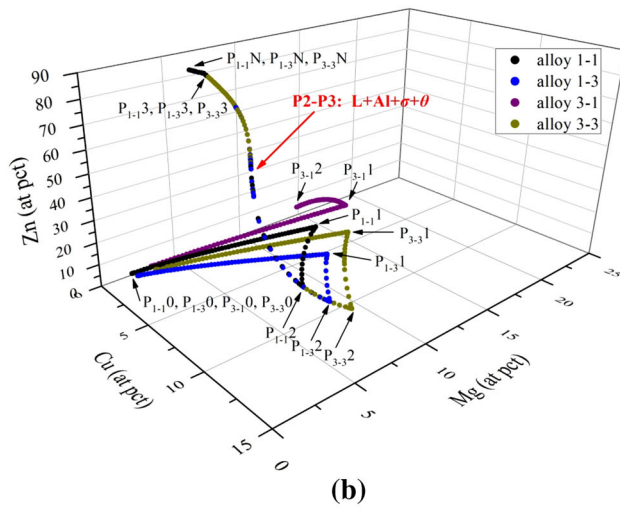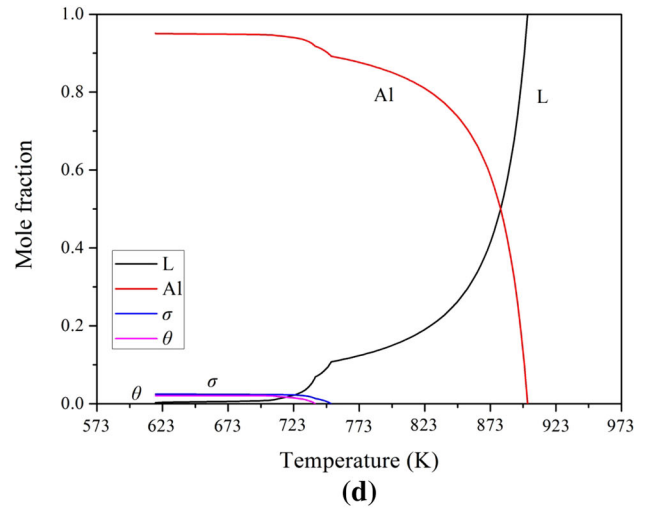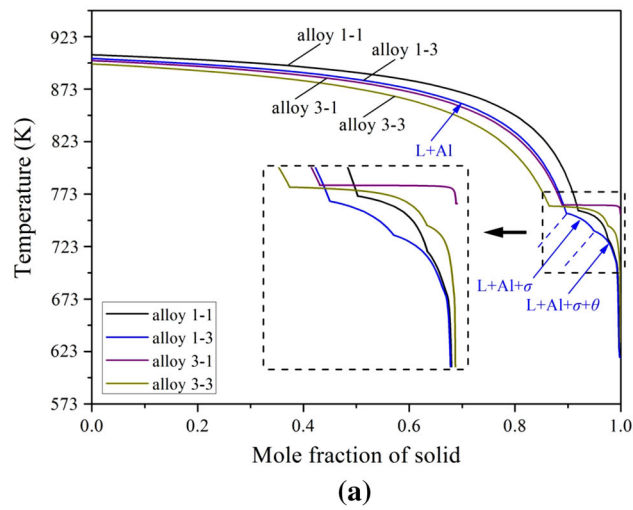
Fig. 4—Calculated results of several typical alloys about solidification in the Scheil model. (*a*) Solidification paths of alloys 1-1, 1-3, 3-1, and 3-3; (*b*) composition evolutions in the liquids of alloys 1-1, 1-3, 3-1, and 3-3; (*c*) heat evolutions of alloys 1-4 and 3-1; mole fraction of each phase *vs* temperature plots of alloys (*d*) 1-4 and (*e*) 3-1.
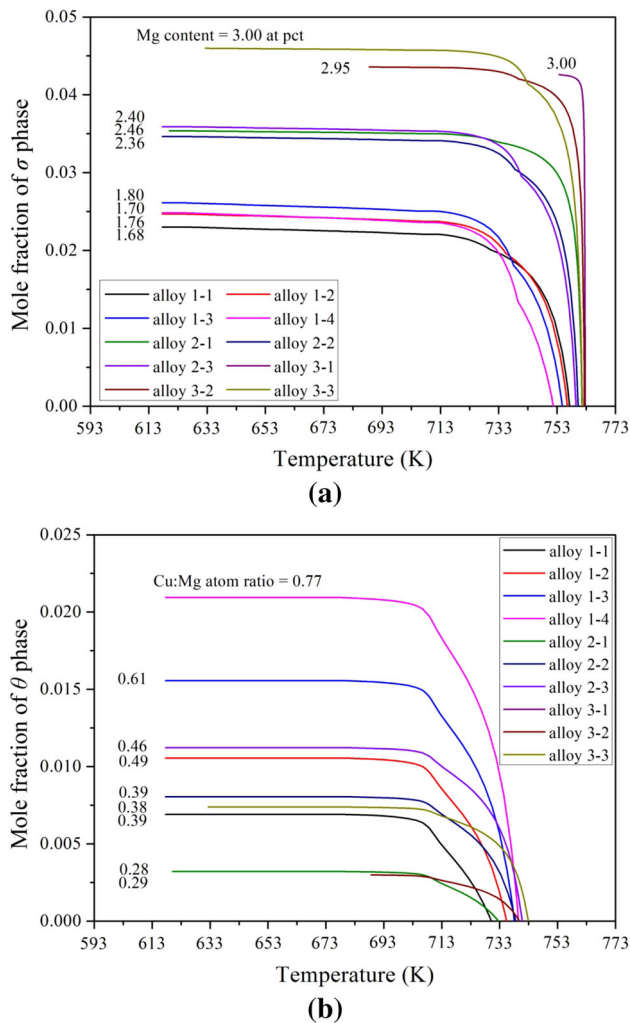
(a)

(b)

Fig. 5—Calculated mole fractions of σ and θ phases *vs* temperature plots for all the alloys in the Scheil model. (*a*) Mole fraction evolution of σ phase and (*b*) mole fraction evolution of θ phase.

Liq. $\rightarrow$ Al, Liq. $\rightarrow$ Al $+ \sigma$, and Liq. $\rightarrow$ Al $+ \sigma + \theta$ can be seen clearly for alloy 1-4. However, for alloy 3-1 the reaction Liq. $\rightarrow$ Al $+ \sigma + \theta$ does not occur during the solidification. The calculated mole fractions of the phases in alloys 1-4 and 3-1 during solidification in the Scheil model shown in Figures 4(d) and (e) indicate that much more σ phase can be formed in alloy 3-1 than that in alloy 1-4, but no θ phase is formed in the former one.

To further reveal the effects of Mg and Cu elements on the types and contents of the phases that formed during solidification, the evolutions of the mole fractions of σ and θ phases formed during solidification in the Scheil model are shown in Figure 5. Apparently, the calculated mole fraction of σ phase is determined and increased primarily by Mg content and secondarily by Cu content, whereas the calculated mole fraction of θ phase is mainly determined and increased by the Cu:Mg ratio. Furthermore, the calculated mole fractions of the σ phase formed during the whole solidification as well as the $(\sigma + \theta)$ phases formed during the eutectic reaction Liq. $\rightarrow$ Al $+ \sigma + \theta$ in the Scheil model are compared

with the measured ΔH_R associated with the dissolution of the massive σ phase and the $(\sigma + \theta)$ pockets of the as-cast alloys during the DSC tests (Table III), respectively, as shown in Figure 6 (because the amount of σ phase dissolved in Peak I is much smaller than that in Peak II in Figure 3(b), the calculated mole fraction of the σ phase formed during the whole solidification is simply compared with the measured ΔH_R associated with Peak II). It can be seen that the regularity in how the Mg and Cu contents affect the phase contents of the as-cast alloys based on the simulation is generally consistent with that obtained from the experiments. Because Mg and Cu are important constituent elements of the σ phase, especially Mg element (considering the semistoichiometric composition of Mg(Zn,Al,Cu)$_2$ as well as the sublattice of MgZn$_2$), the alloys with higher Mg content can form more σ phase during solidification, and Mg also shows a much more significant effect on the amount of σ phase than Cu. Table IV shows the calculated (in the Scheil model) mole fractions and compositions of the liquids before starting the eutectic reaction Liq. $\rightarrow$ Al $+ \sigma + \theta$. The following observations were made:

1. With increasing Mg content, the mole fraction of the liquid is decreased obviously, while high Cu content can increase the mole fraction of the liquid especially for the alloys with low Mg content.
2. High Cu content can increase the Cu content of the liquid slightly.

Consequently, the alloys with low Mg and high Cu contents can have much more liquids and Cu atoms available for the eutectic reaction Liq. $\rightarrow$ Al $+ \sigma + \theta$, and more $(\sigma + \theta)$ pockets can be obtained (θ phase is the main product in this reaction, as shown in Figure 6(b)).

Meanwhile, some discrepancies can also be found between the experimental and the simulated results as shown in Figure 6.

1. The effect of the Cu:Mg ratio on the final amount of the $(\sigma + \theta)$ pockets is slightly overestimated by the simulation, and the experimental results show that Mg content is a crucial factor that determines the amount of the $(\sigma + \theta)$ pockets.
2. For alloy 1-4 the extent of the eutectic reaction Liq. $\rightarrow$ Al $+ \sigma$ is underestimated, while the extent of the eutectic reaction Liq. $\rightarrow$ Al $+ \sigma + \theta$ is overestimated by the simulation. The reasons for the phenomenon 1 and 2 are not quite clear and more work need to be done.
3. The calculated results show that alloys 2-1, 3-2, and 3-3 can form θ phase during solidification, but no θ phase is found in their as-cast alloys. This may be due to the specialty of the basic Scheil model, which neglects the effects of the factors such as back diffusion and coarsening. The calculation in the Scheil model always predicts all possible phases until the lowest eutectic temperature, but in fact, the last phases predicted are often not observed experimentally.[39]

The solidification simulation in the Lever rule is completely different from the simulation in the Scheil model. In the Lever rule, an infinitely slow solidification process and completely global equilibrium are assumed.
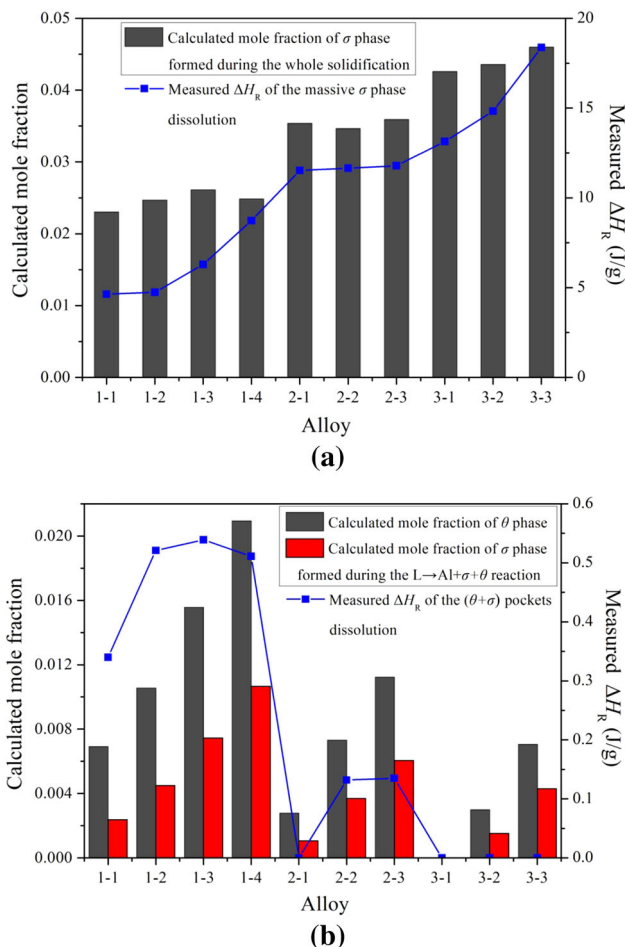
(a)

(b)

Fig. 6—Comparison between the calculated mole fractions of the σ phase formed during the whole solidification as well as the $(\sigma + \theta)$ phases formed during the eutectic reaction Liq. $\rightarrow$ Al + σ + θ in the Scheil model and the ΔH_R associated with the dissolution of (a) the massive σ phase and the (b) $(\theta + \sigma)$ pockets of the as-cast alloys during the DSC test.

Both the Lever rule and the Scheil model simulations are two limiting cases, between which a real solidification path would be expected.[40] To illustrate this situation more clearly, Figure 7 shows the comparison of the solidification paths of alloys 2-1, 2-2, and 2-3 calculated in the Lever rule and the Scheil model, which reveals quite different solidification paths in the two cases. In the Lever rule simulation, neither σ nor θ phase can be formed during solidification in all the three alloys, and this can be easily understood with a calculated isopleth, as shown in Figure 8. While in the Scheil model simulation, σ and θ phases are formed in all the three alloys; moreover, the freezing temperature ranges are much wider (about twice) than those in the Lever rule simulation. The statistical results of the phase components of the designed alloys obtained after the real solidification and the simulated solidification are shown in Table V. Table V indicates that the experimental results fall in between the Scheil and the equilibrium conditions, and close to the former. Considering that, in the Scheil model the calculated mole fractions of the initial liquids available for the eutectic reaction Liq. $\rightarrow$ Al + σ + θ and the final reaction products
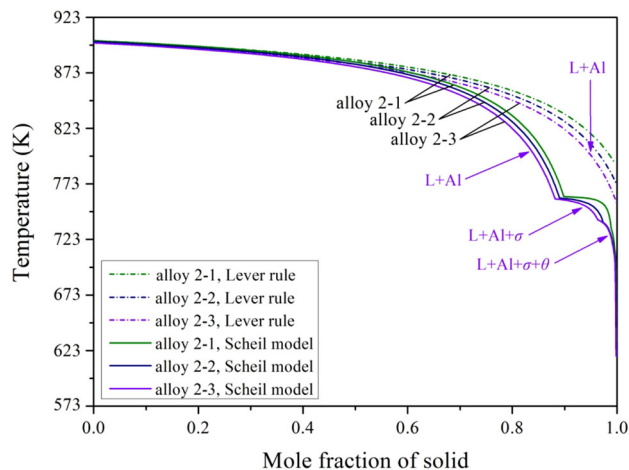
Fig. 7—Calculated solidification paths of alloys 2-1, 2-2, and 2-3 in the Scheil model and the Lever rule.

Table IV. Calculated Mole Fractions and Compositions of the Liquids Before Starting the Eutectic Reaction Liq. $\rightarrow$ Al + σ + θ in the Scheil Model

| Alloy | Composition of the Liquid (At. Pct) | | | | Mole Fraction of the Liquid | Product of Cu Content and Mole Fraction of the Liquid (At. Pct) |
	Al	Zn	Mg	Cu		
1-1	59.74	23.88	5.21	11.17	0.024	0.268
1-2	62.11	20.34	5.75	11.80	0.035	0.413
1-3	63.25	18.50	6.13	12.12	0.051	0.618
1-4	63.84	17.51	6.37	12.28	0.069	0.847
2-1	60.88	22.22	5.43	11.47	0.011	0.126
2-2	63.44	18.21	6.19	12.16	0.027	0.328
2-3	64.38	16.59	6.60	12.43	0.037	0.460
3-1	–	–	–	–	–	–
3-2	63.94	17.34	6.41	12.31	0.010	0.123
3-3	65.24	15.01	7.06	12.69	0.024	0.305
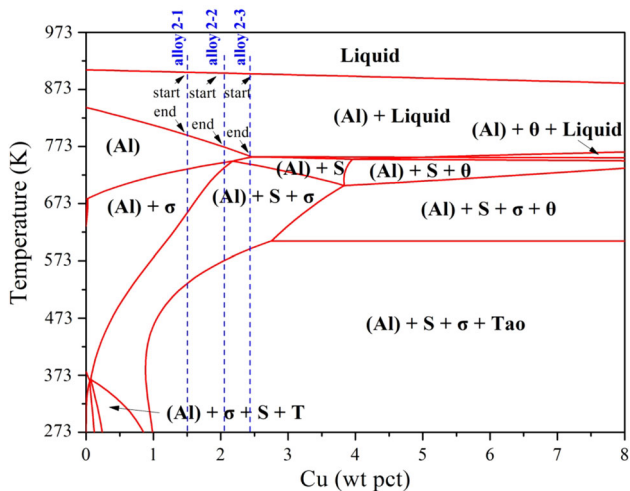
Fig. 8—Calculated isopleth of Al-Zn-Mg-Cu system with 8.5 wt pct Zn and 2 wt pct Mg.

Table V. Phase Components of the Designed Alloys in Different Solidification Conditions (Al₃Zr is not Considered)

Alloy	Lever Rule	Experiment	Scheil Model
		Phase Component	
1-1	(Al)	(Al) + σ + θ	(Al) + σ + θ
1-2	(Al)	(Al) + σ + θ	(Al) + σ + θ
1-3	(Al)	(Al) + σ + θ	(Al) + σ + θ
1-4	(Al)	(Al) + σ + θ	(Al) + σ + θ
2-1	(Al)	(Al) + σ	(Al) + σ + θ
2-2	(Al)	(Al) + σ + θ	(Al) + σ + θ
2-3	(Al)	(Al) + σ + θ	(Al) + σ + θ
3-1	(Al)	(Al) + σ	(Al) + σ
3-2	(Al)	(Al) + σ	(Al) + σ + θ
3-3	(Al) + σ	(Al) + σ	(Al) + σ + θ

(*e.g.*, θ phase) in alloys 2-1, 3-2, and 3-3 are very small (Table IV; Figures 5 and 6), the solidification paths in the Scheil model agree well with the experimental results.

B. Microstructures and Phase Components After Homogenization

1. Homogenization at 733 K (460 °C)

With single-step homogenization [733 K (460 °C)/ 24 hours], the dendritic-network structures in the as-cast alloys 1-1, 1-3, 3-1, and 3-3 are basically eliminated (Figure 9), and the grain boundaries become thinner. Some grains with small sizes (50 to 100 μm) can be distinguished clearly; thus, the average grain sizes of the homogenized alloys seem to be smaller than those of the as-cast alloys. Moreover, the grain refinement with increasing amount of solutes (especially Mg solute) can be seen more clearly from the homogenized alloys.

After the single-step homogenization, the eutectic structures along grain boundaries disappear in the alloys with low or middle Mg content (*e.g.*, ~1.5 and 2.0 wt pct), but some eutectic structures still remain in the alloys with high Mg content (*e.g.*, ~2.5 wt pct),

which have a high content of original (Al + σ) eutectic (Figure 10, Table III). The compositions of the marked phases in Figure 10 are shown in Table VI. According to the SEM observation, alloys 1-1, 1-2, 1-3, and 2-1 have been homogenized fully (the unsoluble Al₇Cu₂Fe phase is not considered here) after the homogenization. Only σ phase exists in alloys 2-2, 3-1, 3-2, and 3-3 after the single-step homogenization. For alloy 1-4, the σ and θ phases that existed in the as-cast alloy disappear, but a new gray phase with composition closing to stoichiometric Al₂CuMg arises, which can be further identified as S phase by the DSC analysis below. This is consistent with the studies about low-Zn Al-Zn-Mg-Cu alloys,[10,28] which revealed the σ-S phase transformation during homogenization. In Figure 10(g), both σ and S phases appear in alloy 2-3 after the single-step homogenization. The XRD patterns of the single-step homogenized alloys show only Al diffraction peaks for all the alloys except alloy 3-3 (Figure 11(a)), and for alloy 3-3, the diffraction peaks about σ phase can still be found. No diffraction signals about σ or S phase can be found in Figure 11(a) for the homogenized alloys 1-4, 2-2, 2-3, 3-1, and 3-2 because of the small concentrations.

From the DSC curves (Figure 11(b)) of the single-step homogenized alloys as well as the corresponding T_P and ΔH_R (Table VII), it is found that for alloys 1-1, 1-2, 1-3, 1-4, and 2-1, the endothermic peaks related to the melting of the (Al + σ + θ) and/or (Al + σ) eutectic disappear, but for alloy 1-4 a new endothermic peak (Peak III) is formed, which can be identified as S phase dissolution according to its T_P [759 K (486 °C)].[10,28,41] For alloys 2-2, 3-1, 3-2, and 3-3, only Peak II representing the dissolution of σ phase can be seen, but the corresponding ΔH_R is reduced greatly compared with the as-cast alloys. For alloy 2-3, both Peak II and Peak III can be seen, indicating the existence of σ and S phases. Obviously, the information from the DSC curves is consistent with the SEM observation.

According to the results above, the alloys with relatively low Mg or low (Mg + Cu) content (*e.g.*, alloys 1-1, 1-2, 1-3, and 2-1) can be homogenized adequately by the single-step homogenization; however, the alloys with relatively high Mg or (Mg + Cu) content (*e.g.*, alloys 1-4, 2-2, 2-3, 3-1, 3-2, and 3-3) cannot be homogenized adequately by this treatment. During the homogenization process, the θ phase is dissolved completely, the σ phase is reduced greatly, and the S phase is formed in some alloys. The formation of the S phase can only be observed in certain alloys with high Cu content (*e.g.*, alloys 1-4 and 2-3), while no S phase can be found in other alloys, which also cannot be homogenized fully. This phenomenon will be further studied in the following text.

The σ-S phase transformation during homogenization has been observed in many studies,[10,18,28,42–45] and a detailed discussion about this transformation at 733 K (460 °C) in AA 7050 and AA 7010 Al alloys was given in References 18 and 28. However, all these studies are about relatively low-Zn Al-Zn-Mg-Cu alloys (*e.g.*, AA 7050, AA 7010, AA 7150, and AA 7085 Al alloys) with 5.87 to 7.81 wt pct Zn. Recently, some research about high-Zn Al-Zn-Mg-Cu alloys (8.10 to 9.97 wt pct Zn)
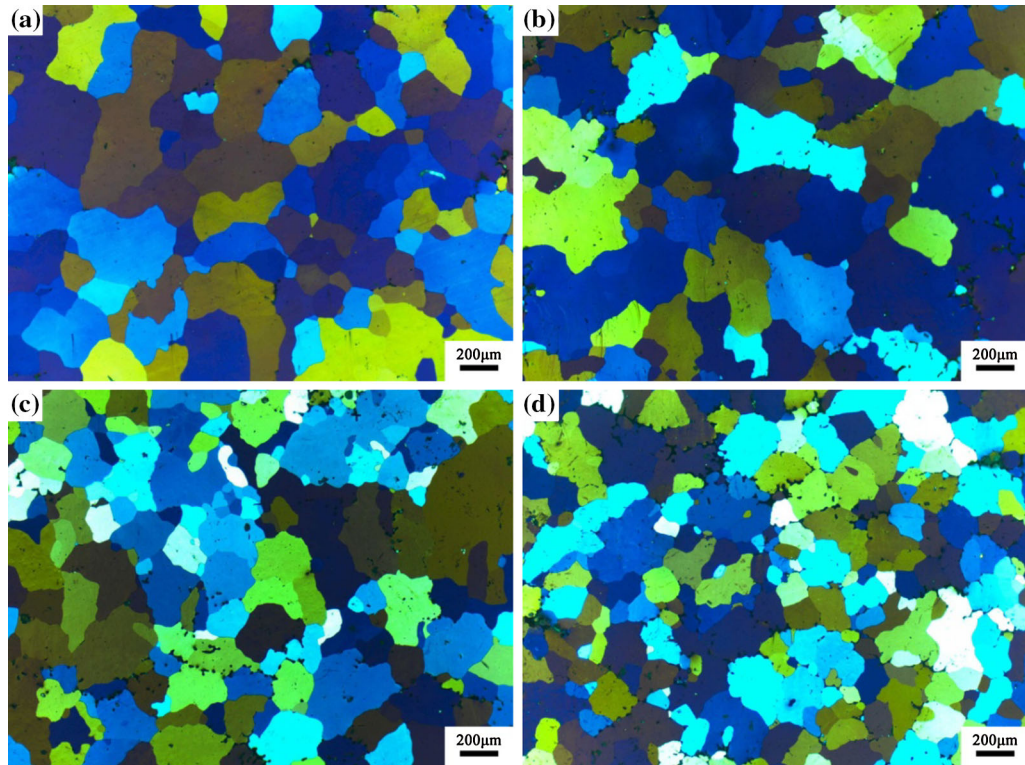
Fig. 9—Color micrographs (in transverse section) of the single-step homogenized [733 K (460 °C)/24 h] alloys. Alloys (*a*) 1-1, (*b*) 1-3, (*c*) 3-1, and (*d*) 3-3.

Table VI. Chemical Compositions (Atmospheric Percent) of the Intermetallic Phases in Fig. 10

Alloy	Phase Marks	Mg	Al	Cu	Zn	Fe	Identified Phase
1-1	A	2.40	77.10	13.64	1.46	5.40	Al_7Cu_2Fe
1-2	B	0.82	71.58	18.22	0.96	8.42	Al_7Cu_2Fe
	C	0.83	70.53	18.84	0.61	9.18	Al_7Cu_2Fe
1-3	D	2.45	82.37	9.80	1.27	4.11	Al_7Cu_2Fe
1-4	E	2.26	80.89	10.35	1.21	5.30	Al_7Cu_2Fe
	F	24.89	56.62	16.93	1.56	—	S
2-1	G	1.42	70.92	18.16	0.77	8.74	Al_7Cu_2Fe
2-2	H	33.29	28.51	16.23	21.96	—	σ
2-3	I	23.68	53.62	20.72	1.98	—	S
	J	34.71	28.48	15.98	20.83	—	σ
3-1	K	31.19	29.87	15.12	23.82	—	σ
3-2	L	34.52	29.70	14.43	21.34	—	σ
3-3	M	33.02	28.75	16.55	21.68	—	σ
	N	32.82	26.78	18.77	21.64	—	σ

shows a different phenomenon that only σ phase remains after the [733 K (460 °C)/24 hours] homogenization, and no σ-S phase transformation is found.[46–48] Even if the heat treatments are performed at higher temperatures [738 K to 748 K (465 °C to 475 °C)], the same results are obtained.[46,47,49] Considering the various phase components of alloys 1-4, 2-2, 2-3, 3-1, 3-2, and 3-3 after the [733 K (460 °C)/24 hours] homogenization, a long-time homogenization [733 K (460 °C)/168 hours] was designed to achieve the phase components of the alloys in the thermodynamic equilibrium state at 733 K (460 °C). The holding time (168 hours) is determined by the diffusion kinetics of

Cu having the lowest diffusion rate among the three main alloying elements, and the related information is shown in Figure 12(a). It is noteworthy that the calculated result based on more appropriate diffusion parameters shows that 168 hours is much longer than the required time for complete homogenization at 733 K (460 °C), and 30.3 hours is enough for all alloys, as shown in Figure 12(b).

The corresponding microstructures of the alloys after the long-time homogenization are shown in Figure 13 with compositions of the marked phases in Table VIII. Compared with the results after the [733 K (460 °C)/ 24 hours] homogenization, S phase is dissolved in alloy
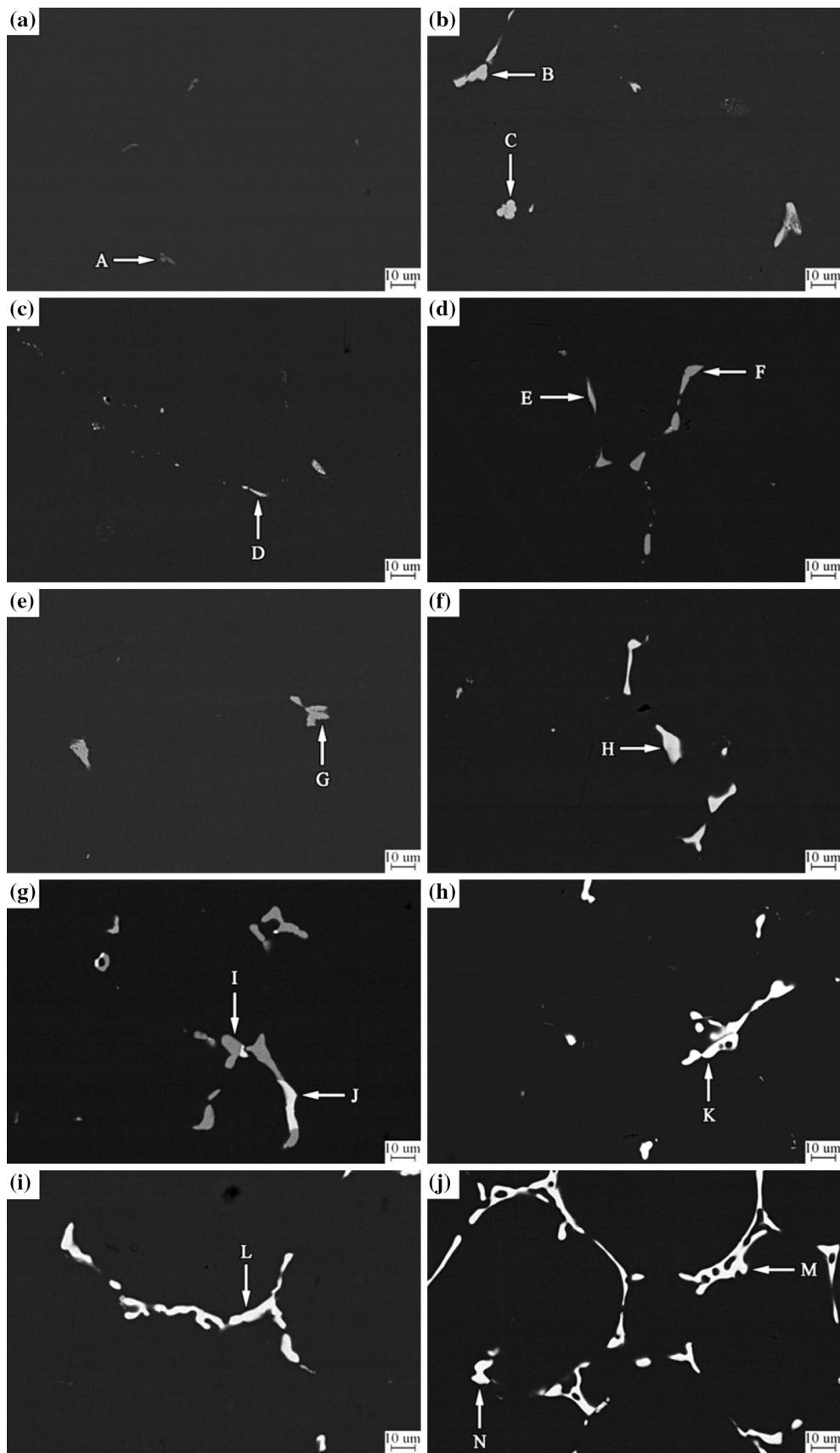
Fig. 10—SEM images (in transverse section) of the single-step homogenized [733 K (460 °C)/24 h] alloys. Alloys (*a*) 1-1, (*b*) 1-2, (*c*) 1-3, (*d*) 1-4, (*e*) 2-1, (*f*) 2-2, (*g*) 2-3, (*h*) 3-1, (*i*) 3-2, and (*j*) 3-3.

1-4 but it remains in alloy 2-3. σ phase exists in alloys 2-2, 3-1, 3-2, and 3-3; meanwhile, S phase arises in alloy 3-3 during the treatment. Therefore, it can be esti-mated that in the thermodynamic equilibrium state at 733 K (460 °C), alloys 1-1, 1-2, 1-3, 1-4, and 2-1 are in single-Al phase field, alloy 2-2, 3-1 and 3-2 are in the (Al + σ) phase field, alloy 2-3 is in the (Al + S) phase field, and alloy 3-3 is in the (Al + σ + S) phase field.

2. *Homogenization at 748 K (475 °C)*

The single-step homogenization [733 K (460 °C)/ 24 hours] cannot promote the complete homogenization of alloys 1-4, 2-2, 2-3, 3-1, 3-2, and 3-3. Therefore, a two-step homogenization [733 K (460 °C)/24 hours + 748 K (475 °C)/24 hours] was designed [in terms of diffusion kinetics, the holding time (24 hours) at 748 K (475 °C) is enough, as shown in Figure 12(b)]. Figure 14 and Table IX show that alloys 1-4, 2-2, and 3-1 are homogenized fully after the two-step homogenization; however, little S phase in alloy 2-3, little σ phase in alloy 3-2, and some (σ + S) phases in alloy 3-3 can still be found. Furthermore, some typical eutectic structures of as-cast alloys, as shown in Figures 1(f) and 2(b), remain in alloy 3-3 after the two-step homogenization, as shown in Figures 14(f) and (g). According to the DSC curves of the two-step homogenized alloys (Figure 15) and the related parameters (Table VII), it is clear that the DSC results are consistent with the SEM observation above. Therefore, it can be estimated that in the thermodynamic equilibrium state at 748 K (475 °C), alloys 1-1, 1-2, 1-3, 1-4, 2-1, 2-2, and 3-1 are in single-Al phase field, alloy 2-3 is in the (Al + S) phase field, alloy 3-2 is in the (Al + σ) phase field, and alloy 3-3 is in the (Al + σ + S) phase field.

Based on the compositions of the intermetallic phases in different conditions as shown in Tables II, VI, VIII, and IX, one can find that the compositions of the σ phase particles retained after different homogenizations are slightly changed compared with those in the as-cast alloys. Correspondingly, the dissolution temperature of σ phase is slightly changed (as shown in Tables III and VII). In addition, the composition of the S phase that formed during homogenization is stable during the heat treatments, and its dissolution temperature is also stabilized at ~761 K (488 °C). In all cases, no obvious effects of alloy design on the compositions of the intermetallic phases can be found.
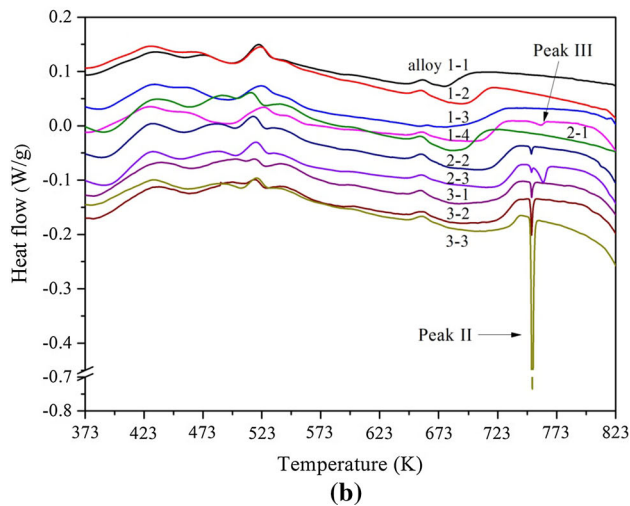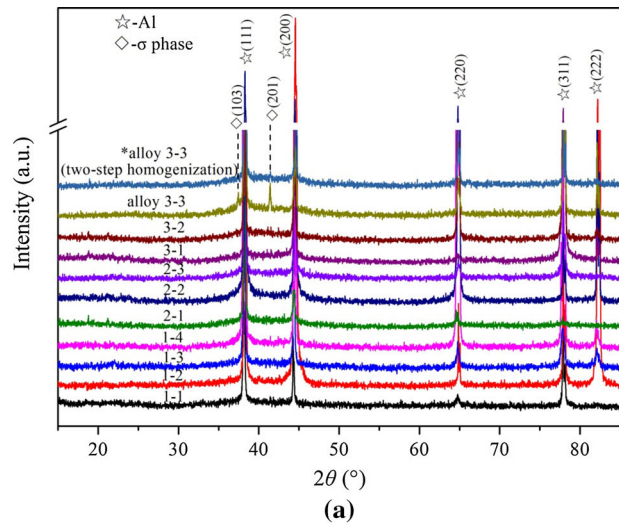

Fig. 11—(a) XRD patterns and (b) DSC curves of the single-step homogenized [733 K (460 °C)/24 h] alloys. [The XRD pattern of alloy 3-3 after the two-step homogenization is also included (a)].

Table VII. Peak Temperature T_P and Heat of Reaction ΔH_R Calculated From the DSC Curves (in Figs. 11(b) and 15) of the Homogenized Alloys

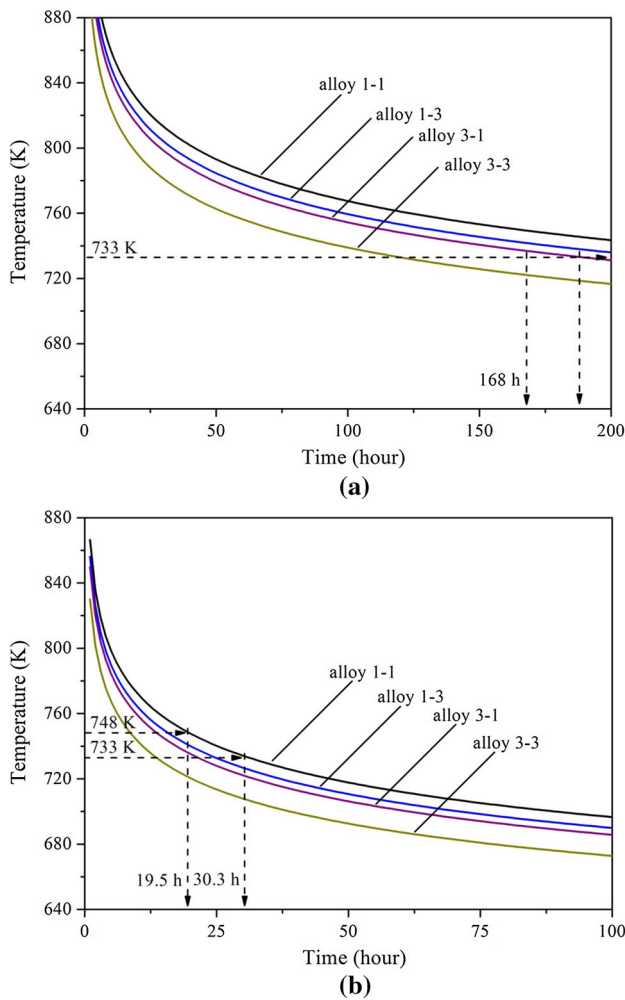|	Single-Step Homogenization				Two-Step Homogenization			
	Peak II		Peak III		Peak II		Peak III	
Alloy	T_P (K)	ΔH_R (J/g)	T_P (K)	ΔH_R (J/g)	T_P (K)	ΔH_R (J/g)	T_P (K)	ΔH_R (J/g)
1-1, 1-2, 1-3, 2-1	—	—	—	—	—	—	—	—
1-4	—	—	759.0	0.298	—	—	—	—
2-2	751.5	0.152	—	—	—	—	—	—
2-3	751.6	0.086	761.6	0.970	—	—	762.2	0.272
3-1	751.7	0.303	—	—	—	—	—	—
3-2	751.6	0.670	—	—	751.5	0.028	—	—
3-3	752.2	5.687	—	—	752.3	0.662	761.0	0.231

Fig. 12—Calculated homogenization temperature *vs* time curves for alloys 1-1, 1-3, 3-1, and 3-3 to achieve the situation that the distribution of Cu atoms is homogeneous with the composition segregation amplitude in the interdendritic regions is reduced to 1 pct. [The calculation was performed according to the equation $\frac{1}{T} = \frac{R}{Q(Cu)} \ln\left(\frac{4\pi^2 D_0(Cu)t}{4.6L^2}\right)$,[10] where T is absolute temperature (K); R is the gas constant, 8.31 J/mol K; $Q(Cu)$ is the activation energy for diffusion about Cu (J/mol); $D_0(Cu)$ is the temperature-independent preexponential about Cu (m²/s); L is the interdendritic spacing of as-cast alloys, which is 112, 100, 93, and 74 μm for alloys 1-1, 1-3, 3-1, and 3-3 respectively.] The calculated results based on (*a*) $D_0(Cu) = 8.4 \times 10^{-6}$ m²/s, $Q(Cu) = 136.8$ kJ/mol,[10,46,50] and (*b*) $D_0(Cu) = 6.5 \times 10^{-5}$ m²/s, $Q(Cu) = 136.0$ kJ/mol.[50–52]

C. Thermodynamic Calculation of the Phase Equilibria at High Temperatures

The calculated isothermal sections of Al-Zn-Mg-Cu phase diagram with 8.5 wt pct Zn at 733 K and 748 K (460 °C and 475 °C) are shown in Figure 16, and the experimental results about the phase components of all the present alloys after the long-time homogenization [733 K (460 °C)/168 hours] and the two-step homogenization [733 K (460 °C)/24 hours + 748 K (475 °C)/24 hours] are added in the isothermal sections. It shows that the experimental results are generally consistent with the calculated results.

In Figure 16(a), it can be seen that, first, Mg content has a great influence on the phase components of the alloys at 733 K (460 °C): The alloys with low Mg content are more likely to be in single-Al phase field, even if the alloys contain high Cu content (*e.g.*, alloys 1-3 and 1-4). According to Lim's research,[15] a high Zn:Mg ratio and low (Mg + Cu) content would be beneficial for obtaining single-Al phase at 733 K (460 °C), and the solubility of Cu can even be increased in the alloys with high Zn:Mg ratio. Also, increasing the Zn:Mg ratio can help to reduce *S* phase during solid-solution treatment.[16] The present alloys 1-1, 1-2, 1-3, 1-4, and 2-1 are satisfied with these composition characteristics, and the experimental results show that the second-phase particles in these five alloys can be dissolved completely at 733 K (460 °C). Second, σ phase is thermodynamically stable at 733 K (460 °C) for the alloys with middle-high Mg and low-middle Cu contents [composition widow: Mg (2.0 to 2.5 wt pct) and Cu (1.5 to 2.0 wt pct)]. The isothermal sections of quaternary Al-Zn-Mg-Cu phase diagram with 6 and 8 wt pct Zn at 733 K (460 °C) in Figure 16(a) show that the (Al + σ) phase field can be expanded greatly toward the composition widow of the commercial 7xxx Al alloys [Mg (1.0 to 2.5 wt pct) and Cu (1.0 to 2.5 wt pct)] with increasing Zn content. Meanwhile, the (Al + *S*) phase field is shrunken obviously by the extended (Al + σ) and (Al + σ + *S*) phase fields. A similar phenomenon can also be found in Reference 53; in brief, the phase component of (Al + σ) in alloys 2-2, 3-1, and 3-2 after the long-time homogenization could be resulted from the high Zn content of the designed alloys and the consequently high thermodynamic stability of σ phase. Third, *S* phase could be thermodynamically stable at 733 K (460 °C) for the alloys with middle-high Mg and high Cu contents [composition window: Mg (2.0 to 2.5 wt pct) and Cu (~2.5 wt pct)]. In this composition range, the alloys with middle Mg content will tend to be in the (Al + *S*) phase field (*e.g.*, alloy 2-3), whereas the alloys with high Mg content will tend to be in the (Al + *S* + σ) phase field (*e.g.*, alloy 3-3).

In Figure 16(b), it can be seen that the dissolution of the second phases are dominated primarily by (Mg + Cu) content at 748 K (475 °C). First, the alloys with (Mg + Cu) $\lesssim$ 4.35 wt pct (*e.g.*, alloys 1-1, 1-2, 1-3, 1-4, 2-1, 2-2, and 3-1) can be in single-Al phase field, which indicates valuable utilization of the great amount of alloying elements [11.46 wt pct ≤ (Zn + Mg + Cu) ≤ 13.04 wt pct]. Second, the alloys with (Mg + Cu) $\gtrsim$ 4.35 wt pct (*e.g.*, alloys 2-3, 3-2, and 3-3) cannot obtain single Al phase. Obviously, high (Mg + Cu) content can make these alloys depart from the single-Al phase field, and the thermal stability of *S* and σ phases would be increased by high Cu and Mg contents, respectively. For these kinds of alloys, the high (Zn + Mg + Cu) content cannot be effectively utilized, and the possible coarse undissolved second-phase particles can decrease the toughness and corrosion resistance.[11,54,55]
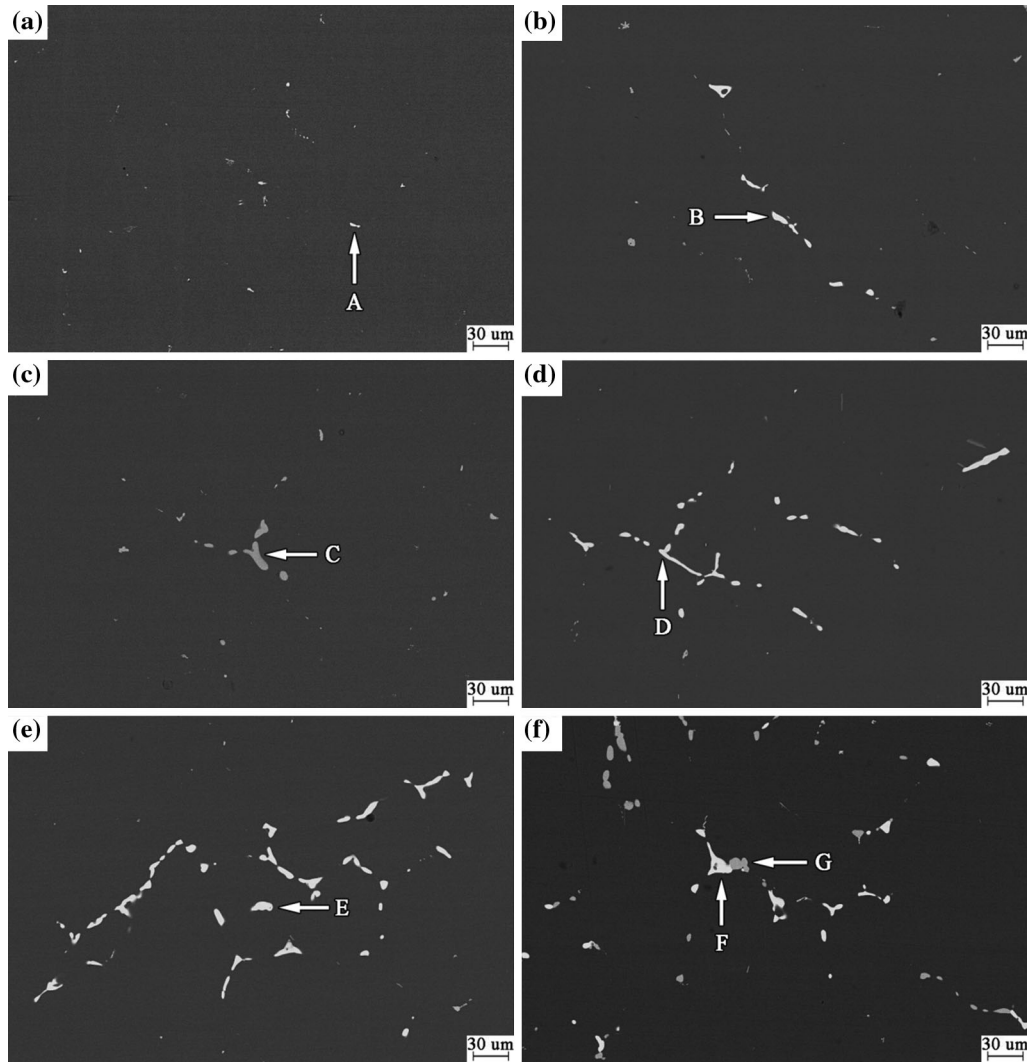
Fig. 13—SEM images (in transverse section) of the long-time homogenized [733 K (460 °C)/168 h] alloys. Alloys (*a*) 1-4, (*b*) 2-2, (*c*) 2-3, (*d*) 3-1, (*e*) 3-2, and (*f*) 3-3.

Table VIII. Chemical Compositions (Atmospheric Percent) of the Intermetallic Phases in Fig. 13

Alloy	Phase Marks	Mg	Al	Cu	Zn	Fe	Identified Phase
1-4	A	2.06	74.79	15.24	1.28	6.63	Al_7Cu_2Fe
2-2	B	32.16	24.71	18.23	24.90	—	σ
2-3	C	24.86	50.61	22.38	2.14	—	S
3-1	D	31.54	25.63	16.05	26.78	—	σ
3-2	E	33.24	26.10	15.76	24.90	—	σ
3-3	F	33.02	25.54	18.54	22.89	—	σ
	G	25.36	49.56	23.19	1.90	—	S

IV. CONCLUSIONS

Presently, the influences of Mg and Cu contents on the solidification paths as well as the phase components at high temperatures of 10 designed Al-Zn-Mg-Cu alloys with high Zn content (about 8.5 wt pct) were systematically studied. The main results are summarized as follows:

1. The primary second phase in all the as-cast alloys is σ phase, while θ phase is prone to exist in the alloys with low Mg and high Cu contents. However,
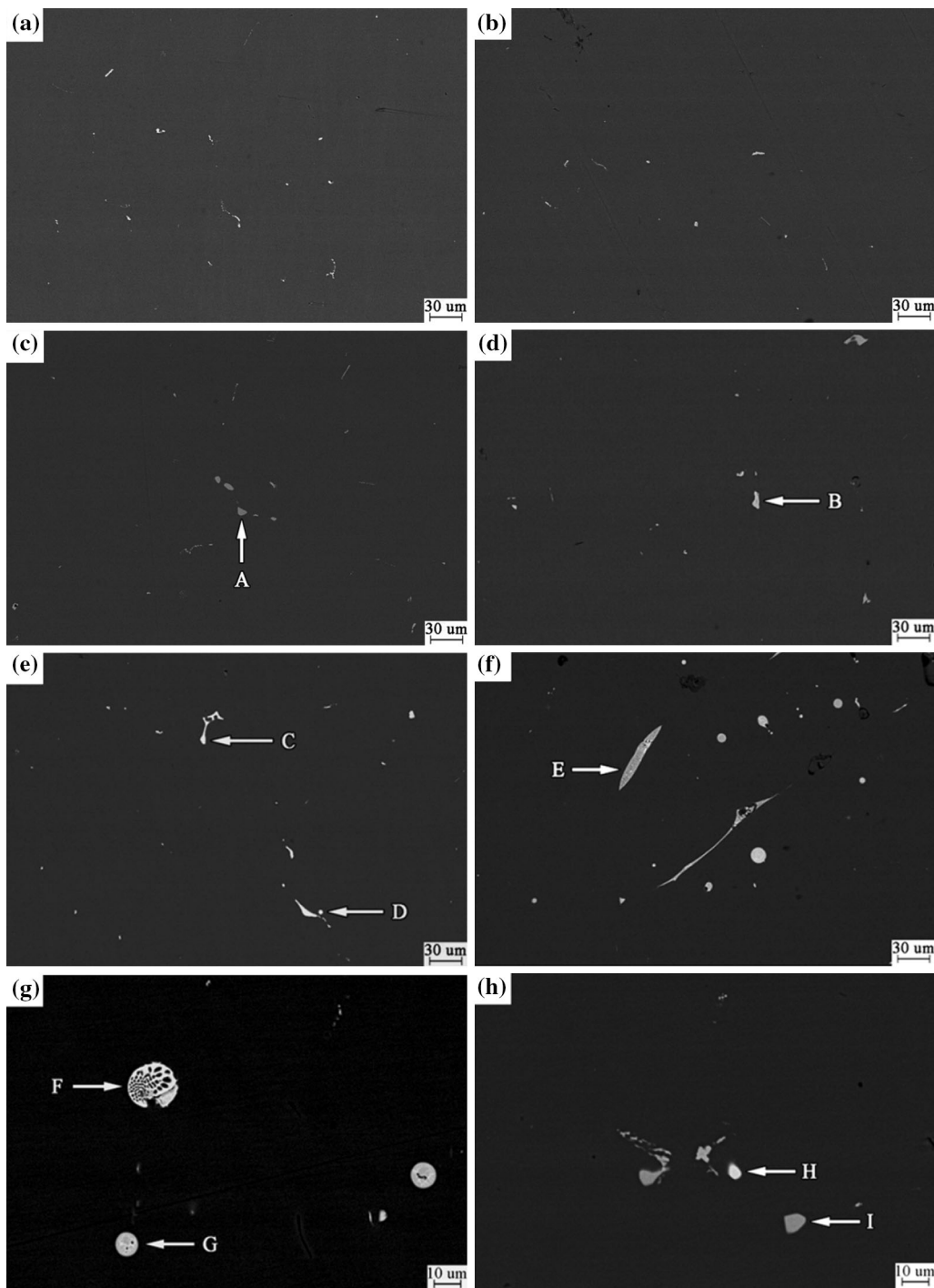
Fig. 14—SEM images (in transverse section) of the two-step homogenized [733 K (460 °C)/24 h + 748 K (475 °C)/24 h] alloys. Alloys (*a*) 1-4, (*b*) 2-2, (*c*) 2-3, (*d*) 3-1, (*e*) 3-2, and (*f*)–(*h*) 3-3.

neither *T* nor *S* phase can be found in all the alloys. The compositions of the intermetallic phases in the as-cast alloys are slightly influenced by alloy design.

2. The real solidification paths of the designed alloys fall in between the Scheil and the equilibrium conditions, and close to the former. The experimental and the simulated results indicate that the amounts of the massive σ phase and the (σ + θ) pockets in the as-cast alloys are determined primarily by Mg content, *i.e.*, the more the Mg content, the more the massive σ phase and the less the (σ + θ) pockets. For the alloys with similar Mg content, the more the Cu content, the

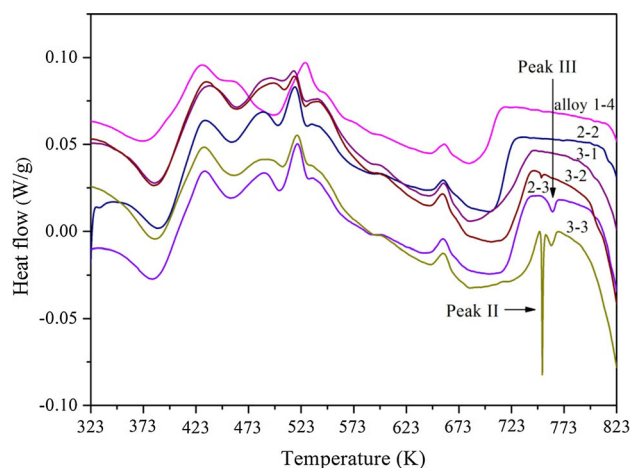| Alloy	Phase Marks	Mg	Al	Cu	Zn	Fe	Identified Phase
2-3	A	25.42	53.99	19.06	1.53	—	S
3-1	B	1.91	71.81	17.55	0.84	8.61	Al_7Cu_2Fe
3-2	C	34.75	31.17	14.23	19.85	—	σ
	D	33.54	29.56	16.26	20.63	—	σ
3-3	E	19.93	61.82	7.94	10.31	—	$(Al + \sigma)$
	F	17.96	57.74	10.35	13.95	—	$(Al + \sigma)$
	G	17.03	57.48	11.86	13.63	—	$(Al + \sigma)$
	H	32.98	27.88	19.52	19.62	—	σ
	I	24.66	50.43	23.04	1.86	—	S

Fig. 15—DSC curves of the two-step homogenized [733 K (460 °C)/24 h + 748 K (475 °C)/24 h] alloys.

more the massive σ phase, generally the more the $(\sigma + \theta)$ pockets. However, it is difficult for the alloys with high Cu content to form $(\sigma + \theta)$ pockets if the alloys contain high Mg content.

3. The phase components of the designed alloys after [733 K (460 °C)/168 hours] and [733 K (460 °C)/24 hours + 748 K (475 °C)/24 hours] homogenizations are generally consistent with the calculated isothermal sections of Al-Zn-Mg-Cu phase diagram with 8.5 wt pct Zn at 733 K and 748 K (460 °C and 475 °C). At 733 K (460 °C), the phase components in the thermodynamic equilibrium state are greatly influenced by Mg content: The alloys with low Mg content are more likely to be in a single-Al phase field, even if the alloys contain a high Cu content. At 748 K (475 °C), the dissolution of the second phases is more effective, and the phase components in the thermodynamic equilibrium state are dominated primarily by (Mg + Cu) content. Except the alloys with (Mg + Cu) $\gtrsim$ 4.35 wt pct, all designed alloys are in single-Al phase field.
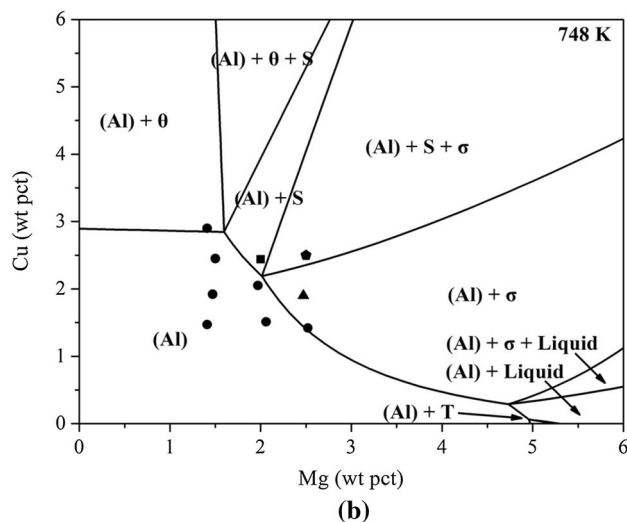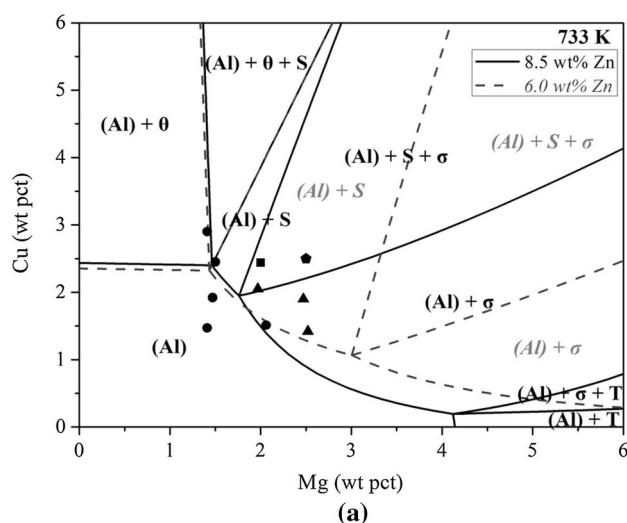

(a)

(b)

Fig. 16—Calculated isothermal sections of Al-Zn-Mg-Cu phase diagram with 8.5 wt pct Zn at (a) 733 K (460 °C) and (b) 748 K (475 °C). [The labeled points with different shapes represent different phase components from the experimental results, round: Al, triangle: Al + σ, square: Al + S, and pentagon: Al + σ + S. In addition, the calculated isothermal section with 6.0 wt pct Zn at 733 K (460 °C) is also included (a)].

REFERENCES

1. E.A. Starke and J.T. Staley: *Prog. Aerosp. Sci.*, 1996, vol. 32, pp. 131–72.
2. J. Liu: *Mater. Sci. Forum*, 2006, vols. 519–521, pp. 1233–38.
3. W.G. Roeseler, B. Sarh, and M.U. Kismarton: *Proceedings of the 16th International Conference on Composite Materials*, 2007.
4. A.S. Warren: *Mater. Forum*, 2004, vol. 28, pp. 24–31.
5. T. Marlaud, A. Deschamps, F. Bley, W. Lefebvre, and B. Baroux: *Acta Mater.*, 2010, vol. 58 (1), pp. 248–60.
6. V. Raghavan: *J. Phase Equilib. Diff.*, 2007, vol. 28 (2), pp. 211–12.
7. N.A. Belov: *Met. Sci. Heat Treat.*, 2012, vol. 53 (9–10), pp. 420–27.
8. Aluminum Association: *International Alloy Designations and Chemical Composition Limits for Wrought Aluminum and Wrought Aluminum Alloys*, The Aluminum Association, Arlington, VA, 2009.
9. D. Dumont, A. Deschamps, and Y. Brechet: *Mater. Sci. Eng. A*, 2003, vol. 356 (1), pp. 326–36.
10. Y. Deng, Z.M. Yin, and F.G. Cong: *Intermetallics*, 2012, vol. 26, pp. 114–21.
11. D.K. Xu, N. Birbilis, D. Lashansky, P.A. Rometsch, and B.C. Muddle: *Corros. Sci.*, 2011, vol. 53 (1), pp. 217–25.
12. F.Y. Xie, X.Y. Yan, L. Ding, F. Zhang, S.L. Chen, M.G. Chu, and Y.A. Chang: *Mater. Sci. Eng. A*, 2003, vol. 355, pp. 144–53.
13. F.H. Gao, G. Zhao, W.M. Bian, and N. Tian: *Mater. Sci. Forum*, 2010, vols. 638–642, pp. 384–89.
14. S.T. Lim, Y.Y. Lee, and I.S. Eun: *Mater. Sci. Forum*, 2005, vols. 475–479, pp. 369–72.
15. S.T. Lim, I.S. Eun, and S.W. Nam: *Mater. Trans.*, 2003, vol. 44 (1), pp. 181–87.
16. X.M. Li and M.J. Starink: *Mater. Sci. Forum*, 2000, vols. 331–337, pp. 1071–76.
17. H.Y. Liang: Ph.D. Thesis, University of Wisconsin-Madison, 1998.
18. X.G. Fan, D.M. Jiang, Q.C. Meng, and Z. Li: *Mater. Lett.*, 2006, vol. 60, pp. 1475–79.
19. L.J. Wang, D.K. Xu, P.A. Rometsch, S.X. Gao, Y. Zhang, Z.B. He, M.J. Couper, and B.C. Muddle: *Mater. Sci. Forum*, 2011, vol. 693, pp. 276–81.
20. C. Mondal and A.K. Mukhopadhyay: *Mater. Sci. Eng. A*, 2005, vol. 391, pp. 367–76.
21. Z.A. Wang, M.P. Wang, W.C. Yang, Q. Zhang, X.F. Sheng, and Z. Li: *J. Mater. Eng.*, 2010, vol. 5, pp. 56–63.
22. C. Zhang, H.B. Cao, G.P. Cao, S. Kou, and Y.A. Chang: *JOM*, 2008, vol. 60 (12), pp. 48–51.
23. H.B. Cao, C. Zhang, J. Zhu, G.P. Cao, S. Kou, R. Schmid-Fetzer, and Y.A. Chang: *Scripta Mater.*, 2008, vol. 58 (5), pp. 397–400.
24. W. Cao, S.L. Chen, F. Zhang, K. Wu, Y. Yang, Y.A. Chang, R. Schmid-Fetzer, and W.A. Oates: *CALPHAD*, 2009, vol. 33 (2), pp. 328–42.
25. W.X. Shu, J.C. Liu, L.G. Hou, H. Cui, J.T. Liu, and J.S. Zhang: *Int. J. Miner. Metall. Mater.*, 2014, vol. 21 (12), pp. 1215–21.
26. J.D. Robson: *Mater. Sci. Eng. A*, 2004, vol. 382, pp. 112–21.
27. R. Ghiaasiaan, X. Zeng, and S. Shankar: *Mater. Sci. Eng. A*, 2014, vol. 594, pp. 260–77.
28. X.G. Fan, D.M. Jiang, Q.C. Meng, B.Y. Zhang, and T. Wang: *Trans. Nonferrous Met. Soc. China*, 2006, vol. 16, pp. 577–81.
29. A.K. Mukhopadhyay, G.M. Reddy, K.S. Prasad, V.K. Varma, and C. Mondal: *Proceedings of the 9th International Conference on Aluminium Alloys*, 2004.
30. A.K. Mukhopadhyay: *Mater. Sci. Forum*, 2012, vol. 710, pp. 50–65.
31. H. Möller and G. Govender: *Sol. St. Phen.*, 2013, vol. 192, pp. 173–78.
32. M. Gazizov, V. Teleshov, V. Zakharov, and R. Kaibyshev: *J. Alloy. Compd.*, 2011, vol. 509 (39), pp. 9497–9507.
33. A.F. Norman, K. Hyde, F. Costello, S. Thompson, S. Birley, and P.B. Prangnell: *MaterSci. Eng. A*, 2003, vol. 354 (1), pp. 188–98.
34. B.H. Zhu: Ph.D. Thesis, General Research Institute for Nonferrous Metals, 2011.
35. Y.A. Chang, S.L. Chen, F. Zhang, X.Y. Yan, F.Y. Xie, R. Schmid-Fetzer, and W.A. Oates: *Prog. Mater. Sci.*, 2004, vol. 49 (3), pp. 313–45.
36. R. Deiasi and P.N. Adler: *Metall. Trans. A*, 1977, vol. 8 (7), pp. 1177–83.
37. X.J. Jiang, B. Noble, V. Hansen, and J. Tafto: *Met. Trans. A*, 2001, vol. 32, pp. 1063–73.
38. Y.A. Chang: *Metall. Mater. Trans. B*, 2006, vol. 37B, pp. 7–39.
39. T. Kraft and Y.A. Chang: *JOM*, 1997, vol. 49 (12), pp. 20–28.
40. S.L. Chen, F. Zhang, S. Daniel, F.Y. Xie, X.Y. Yan, Y.A. Chang, R. Schmid-Fetzer, and W.A. Oates: *JOM*, 2003, vol. 55 (12), pp. 48–51.
41. D.K. Xu, P.A. Rometscha, and N. Birbilis: *Mater. Sci. Eng. A*, 2012, vol. 534, pp. 234–43.
42. N.K. Li and J.Z. Cui: *Nonferrous MetSoc. China*, 2008, vol. 18 (4), pp. 769–73.
43. F.H. Gao, N.K. Li, N. Tian, Q. Sun, X.D. Liu, and G. Zhao: *Trans. Nonferrous Met. Soc. China*, 2008, vol. 18, pp. 321–26.
44. X.L. Han, B.Q. Xiong, Y.A. Zhang, Z.H. Li, B.H. Zhu, and F. Wang: *TransMater. Heat Treat. (China)*, 2010, vol. 31 (11), pp. 104–08.
45. Y.L. Deng, L. Wan, L.H. Wu, Y.Y. Zhang, and X.M. Zhang: *J. Mater. Sci.*, 2011, vol. 46 (4), pp. 875–81.
46. W.B. Li, Q.L. Pan, Y.P. Xiao, Y.B. He, and X.Y. Liu: *Trans. Nonferrous Met. Soc. China*, 2011, vol. 21, pp. 2127–33.
47. Y. Liu, B.H. Zhu, Y.A. Zhang, X.W. Li, H.W. Liu, and B.Q. Xiong: *Chinese JRare Met.*, 2012, vol. 36 (4), pp. 529–34.
48. Y. Han, L. Li, S.Z. Mu, Z.Z. Deng, Y.K. Le, and X.M. Zhang: *Special CastNonferr. Alloy.*, 2010, vol. 30 (10), pp. 891–93.
49. Y.T. Zuo, F. Wang, B.Q. Xiong, Y.A. Zhang, B.H. Zhu, H.W. Liu, and Z.H. Li: *Chin. J. Nonferr. Met.*, 2010, vol. 20 (5), pp. 820–26.
50. Y. Du, Y.A. Chang, B.Y. Huang, W.P. Gong, Z.P. Jin, H.H. Xu, Z.H. Yuan, Y. Liu, Y.H. He, and F.Y. Xie: *Mater. Sci. Eng. A*, 2003, vol. 363, pp. 140–51.
51. W.D. Callister and D.G. Rethwisch: *Materials Science and Engineering: An Introduction*, 7th ed., Wiley, New York, 2007.
52. E.A. Brandes and G.B. Brook: *Smithells Metals Reference Book*, 7th ed., Butterworth-Heinemann, London, 1992.
53. N.A. Belov, D.G. Eskin, and A.A. Aksenov: *Multicomponent Phase Diagrams: Applications for Commercial Aluminum Alloys*, Elsevier, Oxford, 2005.
54. J.A. Wagner and R.N. Shenoy: *Metall. Mater. Trans. A*, 1991, vol. 22A, pp. 2809–18.
55. D.K. Xu, N. Birbilis, and P.A. Rometsch: *Corros. J. Sci. Eng.*, 2012, vol. 68 (3), pp. 035001-1–10.